

Thermodynamic Processes of Perovskite Photovoltaic Devices: Mechanisms, Simulation, and Manipulation

Tianshu Ma, Yidan An, Zhenhai Yang, Zhenhai Ai, Yuqi Zhang, Changlei Wang, and Xiaofeng Li*

Perovskite-based single-junction and tandem solar cells have recently attracted considerable attention due to their remarkable advantages in power conversion efficiency (PCE) and fabrication cost; however, their commercialization remains challenging. One crucial limiting factor is the incompetent thermal management, which is inclined to degrade the PCE and stability of the device. Here, a rigorous opto–electro–thermal (OET) simulation is performed to disclose the internal energy conversion and heat mechanisms within devices. Taking a low-bandgap PSC as an example, the microscopic energy conversion processes concerning the contributions from thermalization, Joule, Peltier, and bulk/interface recombination heats are quantitatively identified. Then various thermal manipulation strategies are proposed, including external (cooling effect) and internal (transport layer materials, photoluminescence colorants, and tandem strategy) methods with the purposes of reducing the heat generation and device temperature. Through the joint OET optimization, the predicted temperature of the considered single-junction (tandem) PSC is reduced to 44.3 °C (33.5 °C) with the possible PCE up to 22.35% (29.08%). Based on the simulation, a tandem PSC (under two-terminal configuration) is fabricated and a PCE of 25.03% is realized. This study offers an effective approach for energy analysis and manipulation to realize higher-performance PSCs with lower operation temperatures.

1. Introduction

Perovskite solar cells (PSCs) have attracted intensive attention in the past decade due to their remarkable advantages in power conversion efficiency (PCE) and fabrication cost. So far, the single-junction PSCs and perovskite/c-Si tandem devices


have recently hit the new certified PCEs of 25.7% and 32.5%,^[1] respectively. To pursue the goal of high-efficient PSCs, various strategies have been proposed to essentially suppress the optical and electrical losses. In detail, through the advanced optical management, such as introducing light-trapping structures or/and antireflection films,^[2,3] and integrating functional materials with low parasitic absorption,^[4] etc., optical potential has been fully unlocked with the optimal short-circuit current density (J_{SC}) values of 26.4 and 20.5 mA cm⁻² for PSC (1.53 eV- E_g) and perovskite/c-Si tandem,^[1,5] respectively, approaching their Shockley–Queisser limits. Moreover, a large number of efforts have been devoted to improving perovskite quality, regulating energy-level, screening/modifying functional materials with the purposes of suppressing bulk/interface non-radiative recombination losses and thus minimizing open-circuit voltage (V_{OC}) deficit and fill factor (FF) loss of related devices.^[6–8] Although many achievements have been made, these types of PSCs still suffer from many inherent

drawbacks in practical application, such as thermal-induced stability and performance degradation, holding back a surplus of chance of commercializing these types of devices.

In terms of the stability of perovskite-based devices, a large body of evidence has been provided to confirm that the generation heat within devices in the working state is bound to accelerate the decomposition of perovskite films by means of heating perovskite lattices,^[9,10] thus reducing the stability of the relevant devices. To address the thermal-induced stability degradation, many attempts have been proposed.^[11] The results showed that the effective thermal management could reduce the heat generation within PSCs and restrain the decomposition of perovskite films, thereby improving the stability of PSCs. In addition, the thermal effect can be directly related to the initial efficiency of PSCs, because a large amount of evidences has confirmed that the effective thermal management could reduce the device temperature and thus raise the device efficiency.^[12] For instance, Zhou et al. reported an innovative method by introducing the silicon dioxide particles with highly thermal conductivity into the hole transport layer (HTL) to serve as the heat dissipation material. As a result, the resultant

T. Ma, Z. Yang, Z. Ai, Y. Zhang, C. Wang, X. Li
School of Optoelectronic Science and Engineering & Collaborative
Innovation Center of Suzhou Nano Science and Technology
Key Lab of Advanced Optical Manufacturing Technologies of Jiangsu
Province & Key Lab of Modern Optical Technologies of Education
Ministry of China
Soochow University
Suzhou 215006, P. R. China
E-mail: xfli@suda.edu.cn

Y. An
Department of Materials Science and Engineering
City University of Hong Kong
83 Tat Chee Avenue, Kowloon, Hong Kong 999077, P. R. China

 The ORCID identification number(s) for the author(s) of this article can be found under <https://doi.org/10.1002/adfm.202212596>.

DOI: 10.1002/adfm.202212596

devices achieve substantially improved long-term stability with the unencapsulated devices maintaining 91%, 95%, and 98% of their initial PCEs after 1126 h of thermal aging, 1235 h of SPO tracking, and 2000 h of ambient aging, respectively.^[13] Apart from the stability, heat generation will inevitably raise the device temperature, which is unfavorable to the device performance especially for V_{OC} and PCE. This conclusion has been widely confirmed in both PSCs and perovskite/c-Si tandems.^[14] For example, Wolf et al. found that perovskite/c-Si tandems can easily reach ≈ 60 °C under direct sunlight in a hot or sunny climate.^[15] The increase of temperature reduces V_{OC} seriously, from 1.74 to 1.54 V within the expected operational temperature range between 25 and 75 °C. In a word, the degradation of device performance especially for V_{OC} in this study, should be attributed to the raised device temperature caused by the heat generation, which is related to the total amount of heats. Therefore, the effective thermal management strategy is of great significance to restrain thermal-induced stability and efficiency degradation for both PSCs and perovskite-based tandems, which, however, requires a comprehensive understanding of heat generation, transport, and dissipation mechanisms to approach their thermodynamic limits.

To address this issue, a large number of theoretical studies have been made.^[16] For instance, Hirst et al. proposed an analytical approach to identify and quantify intrinsic losses of a single threshold cell.^[17] Our group developed a rigorous opto-electro-thermal (OET) model for better understanding of carrier thermodynamic behavior of an SC.^[18,19] In that case, the fundamental thermal effects of an SC including thermalization, Peltier, and Joule heats were clarified and quantified, and many possible manipulation methods including tailoring the doping concentration and energy-level alignment were proposed.^[19] Moreover, we also presented a radiative cooler by the photonic design for a c-Si SC, which demonstrated an absolute improvement in device efficiency of $\approx 0.43\%$ and a reduction in device operating temperature of ≈ 10 °C.^[20] However, it still poses a challenge for us to fully understand the device physics

of thermal behavior especially for PSCs or perovskite-based tandems. Furthermore, a comprehensive thermodynamic manipulation strategy is also urgently needed.

In this work, we address the heat generation, dissipation, and manipulation processes of a PV device via a detailed OET simulation with the purpose of clarifying the intrinsic physical behavior of energy conversion and dissipation. As an example of a low- E_g PSC, the microscopic energy conversion processes due to thermalization, Joule, Peltier, and bulk/interface recombination heats, are elaborated, which suggest that the Peltier and thermalization heats contribute the most to the energy losses. The simulated results reveal that the Peltier losses can be well regulated by tailoring the energy band levels, and the thermalization heats can be reduced from initial 2178 to 194.8 W m⁻² by introducing a down-conversion design. Additionally, a microscopic quantitative analysis for tandem SCs is proposed, suggesting that benefitting from the reduced thermalization loss, a high PCE (>29%) and a low operating temperature (≈ 33.5 °C at MPP) for the tandem PSCs are predicted. Furthermore, guided by the simulation, the single-junction and tandem PSCs were experimentally prepared with the corresponding PCEs of 21.36% and 25.03%, respectively.

2. Results and Discussion

2.1. Energy Conversion Processes

First, we develop a rigorous OET model based on the finite-element method to address and quantify the multi-physics behaviors by coupling the optical, electrical, and thermal modules,^[21,22] where the simulation details are provided in the Supporting Information and the related parameters used for this simulation are listed in Tables S1–S3 (Supporting Information). The microscopic energy conversion processes of photons, charge-carriers, and phonons of a PV cell are illustrated in **Figure 1**, which can be divided into six categories from the

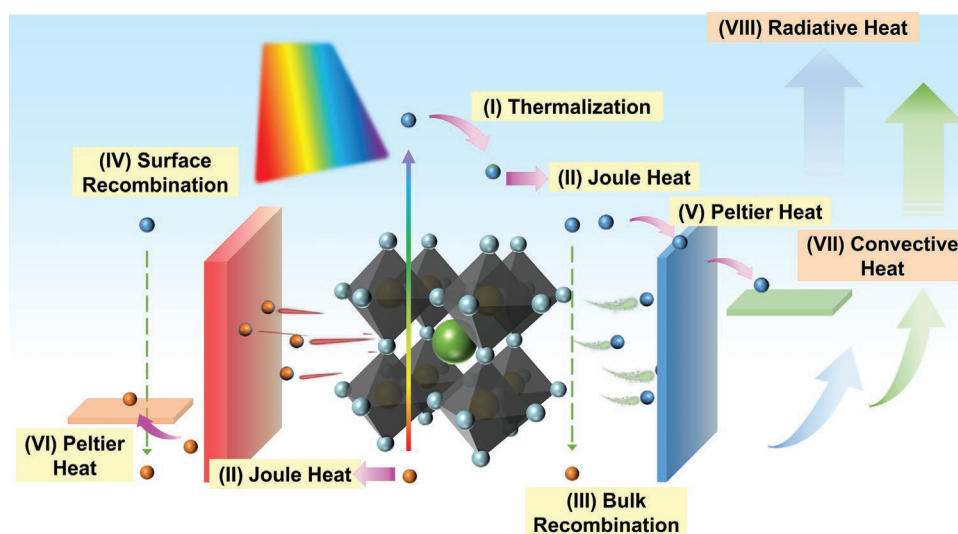


Figure 1. Energy conversion processes of a PV cell concerning: I) thermalization heat, II) Joule heat, III) bulk recombination heat, IV) surface recombination heat, Peltier heat at V) heterojunction interface and VI) metal/semiconductor interface. Heat dissipation processes include VII) convective heat and VIII) radiative heat.

viewpoint of recombination sources: I) thermalization heat arising from the energy relaxation, i.e., photon-excited electrons (holes) with excess potential energy beyond bandgap (i.e., $h\nu - E_g$, where ν is the frequency of incident light) return to the conduction (valence) band edge in picosecond timescales;^[23] II) Joule heat caused by the motion of carriers under built-in electric-field within the depletion region;^[24] III) bulk recombination heat contributing from Shockley–Read–Hall (SRH) and Auger recombinations; it is worth noting that although the radiation recombination is very important for V_{OC} , it is not a source of heat generation, thus we do not discuss the radiation recombination when describing bulk recombination, and the Auger recombination is almost negligible compared with SRH recombination (Figure S1, Supporting Information). IV) surface recombination heat attributed to the carrier trapping effect by surface defects; V) Peltier heat at heterojunction interface due to the energy band offset; and VI) Peltier heat at the semiconductor/metal interface, where the transport carriers have to flow from conduction/valence band of semiconductor region to the quasi-Fermi level before being collected by the respective electrodes.^[25] Moreover, the macroscopic heat exchange processes including convective VII) and radiative VIII) mechanisms are also considered, so that the devices operating temperature can be evaluated precisely.

In this study, we take a tin–lead (Sn–Pb) mixed component perovskite as an example to construct the perovskite devices. Owing to the suitable E_g (i.e., 1.25–1.4 eV), this type of perovskite is a promising alternative for the single-junction PSCs and bottom sub-cells of all perovskite tandems.^[26–28] Specially, an inverted $p-i-n$ PSC consisting of indium-doped tin oxide (ITO), poly(3,4-ethylenedioxythiophene):polystyrene sulfonate (PEDOT:PSS) hole transport layer, (FASnI₃)_{0.6}(MAPbI₃)_{0.37}(MA PbBr₃)_{0.03}, fullerene (C₆₀)/2,9-dimethyl-4,7-diphenyl-1,10-phenanthroline (BCP) electron transport layers, and Ag electrode,^[29] is considered.^[29]

2.2. Energy Analysis of Single-Junction PSCs

Based on the OET model, the macroscopic energy distributions of the single-junction PSCs can be estimated. By performing the optical simulation, the device reflection together with effective/parasitic absorption are investigated. After careful observation from **Figure 2a,b**, we can find that: 1) the presence of the rear-side Ag electrode leads to a strong optical reflection especially at 1.1–4 μm waveband, yielding a power loss of 317.5 W m^{-2} ; 2) benefiting from the high absorption coefficients of perovskite, perovskite layer with a thickness of 850 nm could absorb a high power density of 619.2 W m^{-2} ; 3) the parasitic absorption of ITO (Ag electrodes) at 0.3–0.5 μm (1–2 μm) waveband contributes a power density consumption of 11.5 (51.8) W m^{-2} ; 4) the transport layers show an ignorable optical absorption, which thus is not included in this system. To reveal the microscopic energy conversion processes of this type of PSCs, we then investigate energy distributions under the different operating conditions. In the short-circuit condition, all absorbed powers are completely converted into the unfavorable heat. Detailedly, the power densities for Joule, Peltier, and thermalization processes, i.e., P_{Joule} , P_{Peltier} and

P_{Thermal} , are determined to be 262.7, 136.5, and 217.8 W m^{-2} , respectively. It is worth noting that the bulk and surface recombination losses lead to a neglectable contribution with a power density of only 2.2 W m^{-2} , which is due to that the built-in electric field in the short-circuit condition is strong enough to effectively separate the photogenerated carriers, so that the bulk and surface recombination can be intrinsically suppressed. The bias-dependent energy distributions are presented in **Figure 2c**, which suggest that: 1) P_{Thermal} and P_{Peltier} (i.e., $P_{\text{out}} + P_{\text{Peltier}} + P_{\text{Rec}} + P_{\text{Joule}}$) remain unchanged under the different bias voltages, meaning that the power densities absorbed by PSC and consumed by thermalization are independent of the forward bias; 2) with the increasing of the forward bias from 0 to 0.87 V, P_{Joule} decreases gradually due to the weakened built-in electric-field together with the reduced current density; 3) P_{Rec} is negligible until the forward bias is >0.6 V, which rapidly increases near the V_{OC} owing to fact that the weakened built-in electric-field leads to poor carrier separation and extraction efficiency and thus increases the recombination; 4) P_{Peltier} remains constant until the forward bias is close to V_{OC} ; 5) as a result, the maximal P_{out} at the forward bias of 0.73 V is yielded. The corresponding $J-V$ curve is plotted in **Figure 2d**, where the experimental result with the identical structure is also presented as a reference. Considering the actual working temperature, the simulation results are consistent with that of the experiment one, with J_{SC} of 31.93 mA cm^{-2} (31.73 mA cm^{-2}), V_{OC} of 0.842 V (0.841 V), FF of 78.3% (78.2%), and PCE of 21.05% (20.87%) for the simulation (experiment). The quantitative analysis of thermodynamic behaviors of such a PSC at the maximum power point (MPP) is illustrated in **Figure 2d**. We can find from this figure that the percentages of P_{Thermal} , P_{Joule} , P_{Rec} , P_{Peltier} , and P_{out} at MPP are determined to be 35.18%, 3.78%, 3.09%, 21.9%, and 36.05%, respectively. This means that in terms of the absorbed power of such a low- E_g PSC, only 36.05% power can be used and exported, leaving 63.95% of the power to be dissipated as the heat, in which thermalization and Peltier processes contribute the most. Since a large proportion of energy will be dissipated in the form of heat, the device temperature will thus be raised. We then study the temperature effect on the performance of this type of devices. As demonstrated by the $J-V$ curves in **Figure 2e**, we can find an obvious deterioration in V_{OC} and PCE with the increase of temperature from 10 to 70 °C. This is because for a PV cell, V_{OC} can be expressed as follows:^[30]

$$V_{OC} = \frac{kT}{q} \ln \left(\frac{J_{SC}}{J_0} + 1 \right) \quad (1)$$

$$J_0 = A \times \exp \left(-\frac{E_g}{kT} \right) \quad (2)$$

where q is the electron charge, k is the Boltzmann's constant, T is the temperature, E_g is the bandgap, J_0 is dark saturation current density, and A is the constant. From these equations, we can conclude that increasing device temperature (i.e., T) will lead to a significant increase in dark saturation current density (i.e., J_0), which thus results in a reduced V_{OC} . As for J_{SC} , it is more determined by the number of the generated

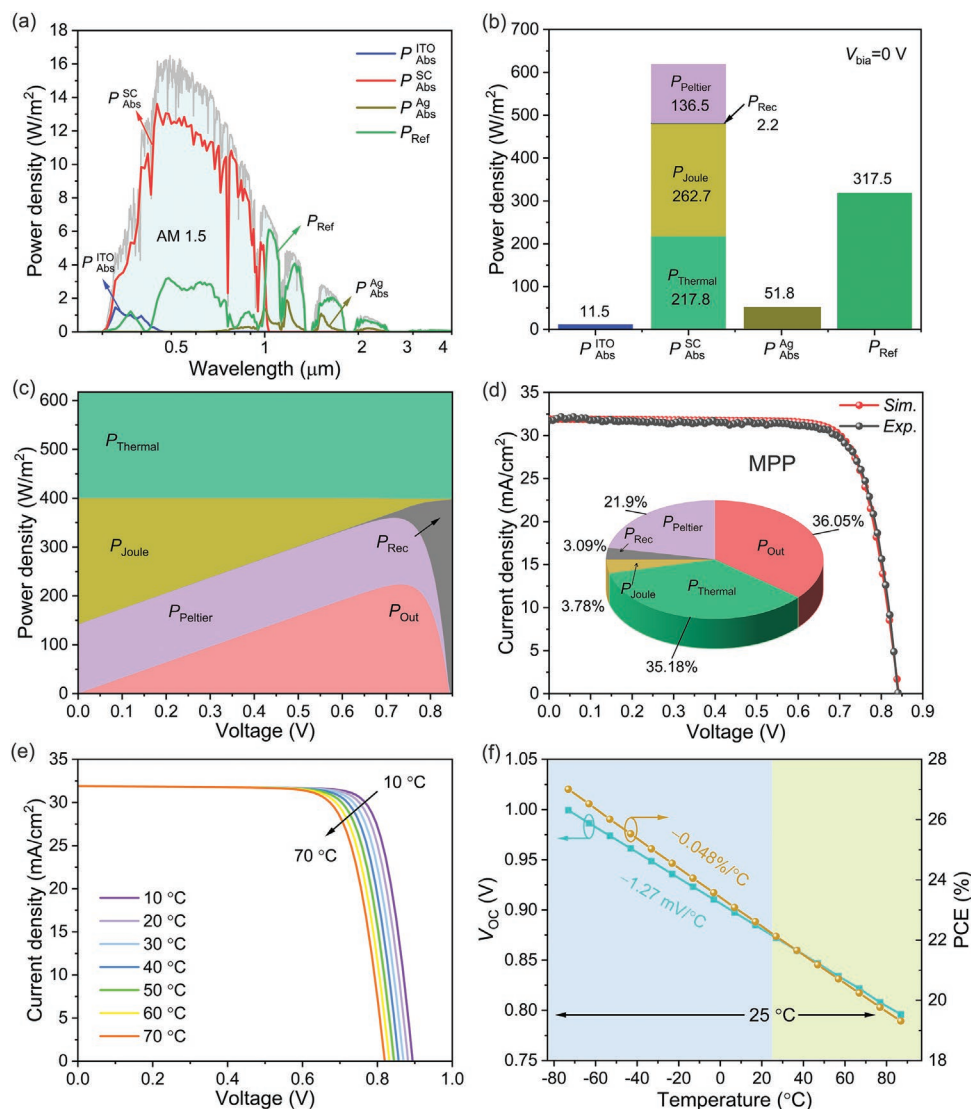


Figure 2. Macroscopic energy analysis and temperature effect of single-junction PSCs. a) Absorbed and reflected power density spectra, where the standard AM 1.5G solar spectrum is also plotted for reference. Here, the P_{Abs}^{SC} , P_{Abs}^{ITO} , and P_{Abs}^{Ag} denote the absorptions of PSC, ITO, and Ag, respectively, and P_{Ref} denotes the reflection of the device. b) Distributions of power density components under the short-circuit condition, where the V_{bias} denotes the external scan voltage. c) Power densities of the different heat conversion contributions as functions of the forward bias. Here, the $P_{Thermal}$, P_{Joule} , $P_{Peltier}$, P_{Rec} , and P_{Out} denote the power densities for thermalization, Joule, Peltier, recombination, and electrical output processes, respectively. d) Simulated and experimental $J-V$ characteristic curves, where the pie chart of microscopic energy conversion components at MPP is inserted. e) Simulated $J-V$ curves of the PSC under the different operating temperatures ranging from 10 to 70 °C. f) V_{OC} and PCE of such a single-junction PSC as a function of operating temperature.

electron-hole pairs within photoactive layers, which, however, is almost independent of temperature. In terms of FF , it depends more on the transport resistance even though it may be slightly affected by temperature. Therefore, increasing the operating temperature has a significant effect on V_{OC} , but little on J_{SC} and FF .^[15] In particular, plots of V_{OC} and PCE as functions of temperature are displayed in Figure 2f, showing a linear decline by factors of -1.27 mV °C⁻¹ and -0.048% °C⁻¹, respectively. Agreeing well with the experimental observation in the reference,^[31] PCE of this type of PSCs shows less dependence on operating temperature in contrast with the conventional Si SCs (-0.055% °C⁻¹).

2.3. Energy Manipulation of Single-Junction PSCs

As discussed above, increasing the operating temperature will degrade the device performance. Here, we propose two effective strategies, i.e., convective and radiative cooling, to accelerate the heat dissipation processes and thus mediate the operating temperature with the corresponding results demonstrated in Figure 3a. Two key parameters, i.e., thermal emissivity (that can be extracted from the integrated absorptivity) and convective coefficient h (that is depended on the wind speeds),^[32] are kept at 0.87 and 12 W m⁻² K⁻¹, respectively. In the presence of the convective and radiative cooling processes, a large number

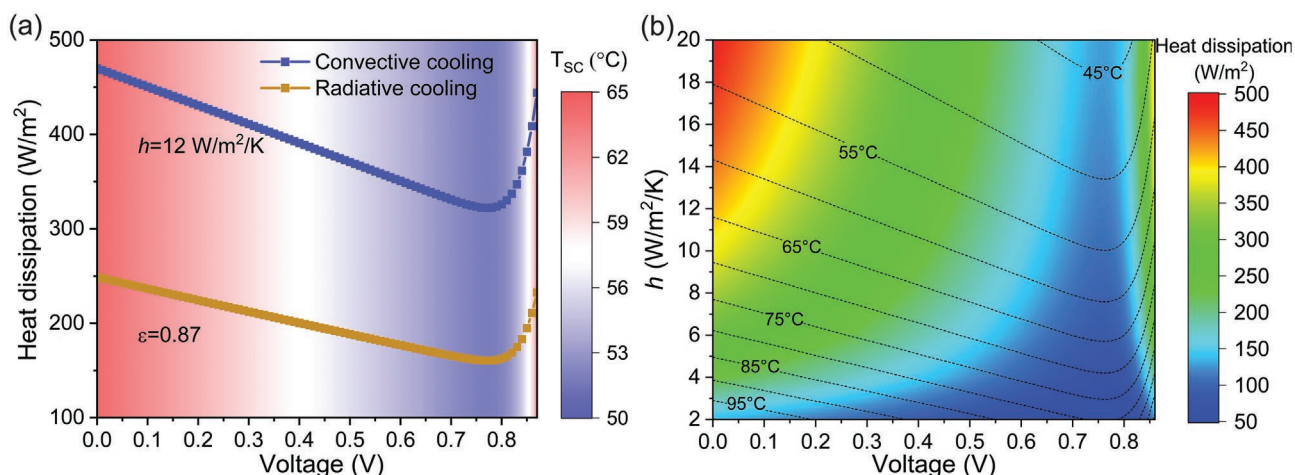


Figure 3. Quantified power density of heat dissipation. a) Heat dissipation power densities with convective cooling and radiative cooling as functions of forward bias, and the corresponding device temperature is also shown in the figure. b) Heat dissipation power densities of PSC versus the forward bias and h , where the temperature contour lines are also marked.

of heats can be effectively dissipated, thus reducing the effect of heat accumulation on device temperature rise (Figure 3a). Owing to that PSC has the maximal power density output (P_{Out}) at MPP, the amount of heat generation in this condition is the least, and a lowest operating temperature thus be expected. Moreover, it is noted that if the two cooling processes are weak enough, the operating temperature of the devices will be $>100\text{ }^{\circ}\text{C}$, demonstrating that the external cooling strategies play a significant role in cooling devices. There are lots of experiments which indicate the existence of this super-high temperature: Wang et al. reported that for a commercial silicon solar cell without the radiative emitters, the device temperature can reach $80\text{ }^{\circ}\text{C}$;^[33] Koehl et al. showed that for the CIGS module, the PV-module temperature can reach $82\text{ }^{\circ}\text{C}$ under an ambient temperature T_{amb} of $20\text{ }^{\circ}\text{C}$ and a wind speed of 1 m s^{-1} , which can increase to $109.3\text{ }^{\circ}\text{C}$ under a higher ambient temperature T_{amb} of $40\text{ }^{\circ}\text{C}$.^[34] The operating temperatures and dissipation powers under the various convective coefficients (h) are then investigated with the corresponding results shown in Figure 3b. If the h is low enough (e.g., $< 4\text{ W m}^{-2}\text{ K}^{-1}$), heat dissipation power density is $<150\text{ W m}^{-2}$, which is too small to effectively release the generated heat into the environment, so that a high working temperature exceeding $70\text{ }^{\circ}\text{C}$ is predicated. For a high h (e.g., $> 18\text{ W m}^{-2}\text{ K}^{-1}$) that can be realized by increasing air flow speed or employing water cooling system, heat dissipation power density increases significantly, suggesting a low working temperature ($\approx 45\text{ }^{\circ}\text{C}$) near MPP.

The above-mentioned discussion is based on a single material system, i.e., PEDOT:PSS and C_{60} /BCP as the HTL and electron transport layers (ETLs), respectively, which, however, imposes restrictions on the understanding of the whole picture of thermal regulation. Here, we focus on a few of typical ETLs including [6,6]-phenyl- C_{61} -butyric acid methyl ester (PCBM), SnO_2 , and C_{60} , as well as HTLs including PEDOT:PSS, poly[bis(4-phenyl)(2,5,6-trimethylphenyl) amine] (PTAA), and NiO_x as shown in Figure 4a.^[35,36] The main electrical parameters of these TL materials are listed in Table S3 (Supporting Information). Since the valance band maximum (VBM) of HTL

and conduction band minimum (CBM) of ETL are particularly important for PSC to regulate their energy levels and performance, PCEs of PSCs under the various ETL CBMs and HTL VBMs are studied as demonstrated in Figure 4b, where the representative ETL/HTL groups are marked in this figure. It can be seen from Figure 4b that a high PCE can be obtained under a large range of ETL CBMs (i.e., from -4.4 to -4.6 eV) and HTL VBMs (i.e., $< -5.2\text{ eV}$). This means that the device PCE can be effectively regulated by tailoring the energy levels of ETLs and HTLs. For a favorable energy-level structure (i.e., ETL CBM and HTL VBM are well-matched with that of perovskite), carriers could be easily extracted free from transport barrier. On the contrary, an unfavorable energy-level structure will impede carrier transport and thus degrade the device PCE.^[37] The regulation of energy levels of ETLs or/and HTLs not only affects the device PCE, but also masters the process of heat generation. Specially, it is widely accepted that Peltier heat is closely related to the energy-level offset of heterojunction interface. The Peltier power distributions under the various ETL CBMs and HTL VBMs are shown in Figure 4c, which reveal that: 1) for the well-matched CBM/VBM between ETL/HTL and perovskite (i.e., $-4.4\text{ eV} < \text{ETL CBM} < -3.9\text{ eV}$ and $-5.6\text{ eV} < \text{HTL VBM} < -5.2\text{ eV}$), a low $P_{\text{Peltier}} < 100\text{ W m}^{-2}$ can be expected; 2) a large energy band offset ($>0.4\text{ V}$) delivers a high P_{Peltier} beyond 300 W m^{-2} ; 3) an obvious position shift of the PCE plateau and P_{Peltier} maximum can be seen, suggesting that a best PCE does not mean a minimal P_{Peltier} and a favorable energy band offset is beneficial for device performance, despite it may lead to a large P_{Peltier} . Moreover, the corresponding P_{Rec} distributions under the typical ETL CBMs and HTL VBMs are also presented as shown in Figure 4d. We can find from these plots that P_{Rec} is limited to 50 W m^{-2} even under a high energy band offset (i.e., $> 0.4\text{ eV}$), but a direct association of P_{Rec} and PCE, i.e., a high PCE is often accompanied by a low P_{Rec} , can be concluded. In addition, the energy band diagrams of PSCs featuring these typical ETLs and HTLs are also illustrated to account for the device PCE and thermal distribution variation induced by energy levels. As can be seen from Figure 4e, device

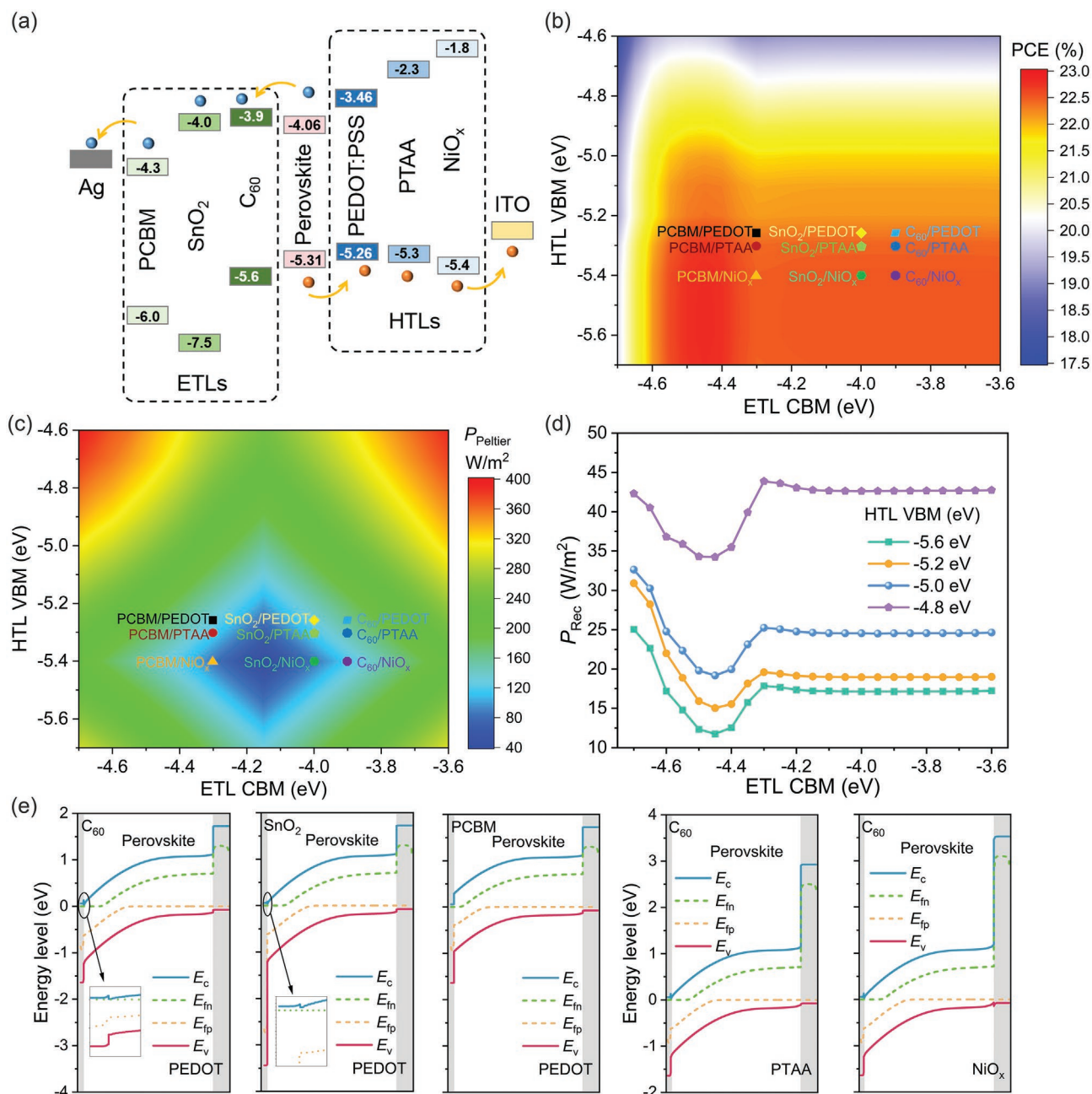


Figure 4. Effects of the different TLs on Peltier heat of single-junction PSCs. a) Conduction and valence band positions of the different ETL and HTL materials. b) PCE and c) Peltier heat contour maps under various ETL CBM and HTL VBM, where the typical ETL/HTL groups are also marked in this figure. d) P_{Rec} plots as a function of ETL CBM under different HTL VBMs. e) Energy band diagrams of PSCs with the typical ETLs and HTLs.

with the PCBM ETL shows a favorable energy band offset with the appearance of forming an energy cliff for electron transport, however, C₆₀ and SnO₂ ETLs produce an energy spike to hinder carrier transport. However, limited by the fabrication process, the PSCs with PCBM ETL do not exhibit a higher device efficiency, which may be due to the relatively poor conductivity and interface passivation of PCBM. Therefore, we use C₆₀ ETL to fabricate PSCs in this study. Although a slight downhill energy band offset for NiO_x HTL is observed, this seems to have less effect on the performance of PSC as compared with

PEDOT:PSS and PTAA HTLs. As a whole, regulating energy level positions of ETLs and HTLs is an effective strategy to mediate the device efficiency and heat conversion.

As mentioned in Figure 2, P_{Thermal} that receives widespread validity as a causal factor for device temperature rise accounts for a large part of energy power in this low- E_g PSC. To suppress P_{Thermal} , we propose a potential down-conversion strategy that could absorb the high-energy photons and convert into visible light to reduce thermalization heat and mediate spectrum response.^[38–40] Here, the YAG:Ce down-conversion material

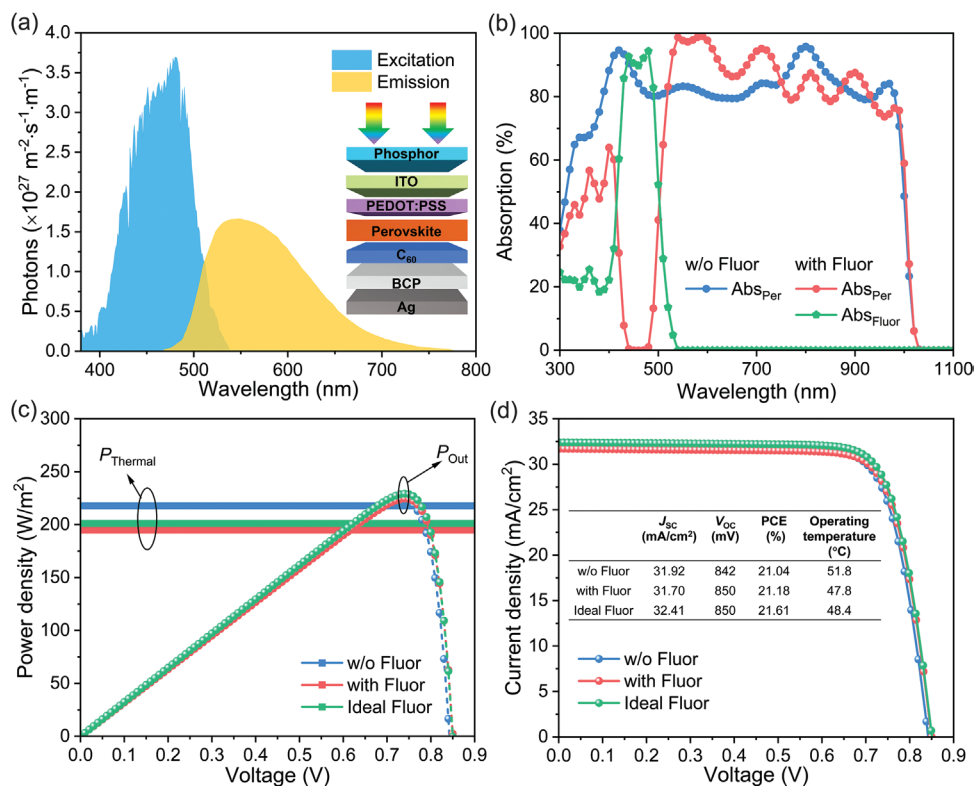


Figure 5. Effects of photoluminescence on heat conversion process of single-junction PSCs. a) Excitation and emission spectra of photoluminescence colorants used for simulation. b) Absorption spectra of devices without and with fluorescent design. c) Thermalization and output power densities, and d) J - V curves for devices without, with real and with ideal fluorescent designs.

is considered, where the corresponding excitation and emission spectra are plotted in Figure 5a.^[41] It is quite clear that an obvious shift in response wavelength can be seen, i.e., 380–550 nm (460–780 nm) for the excitation (emission) spectrum. Fluorescence quantum yield (QY) representing the ratio of the emitted photons to the absorbed photons is considered in this simulation (Figure S2, Supporting Information).^[42,43] In this study, the fluorescent material is put on the top side of ITO to avoid affecting the electrical properties of devices. First, the optical absorption of perovskite layer of the related cases is investigated as shown in Figure 5b. It can be observed that due to the presence of fluorescent material, the absorption of perovskite layer (red line) significantly reduces compared with the counterpart without fluorescent material (blue line) at the waveband of 400–550 nm, which, however, can be compensated from the improved absorption at the wavelength ranging from 550 to 750 nm, where the reflection spectra and reflection power density of these two cases can refer to Figure S3 (Supporting Information). Based on the optical response, P_{Thermal} and P_{Out} of the device with fluorescent design can be calculated as shown in Figure 5c, where the referenced device without fluorescent material is also considered for comparison. It can be found that device with fluorescent design shows a reduced P_{Thermal} , i.e., from 217.8 to 194.8 W m^{-2} . By regulating the thickness of phosphor and screening the suitable fluorescent materials with lower refractive index and higher QY, the P_{Thermal} can be further reduced. The corresponding simulated J - V characteristic curves of these typical PSCs are plotted in

Figure 5d, and the related parameters are extracted and tabled in this figure. Compared with the PSC without fluorescent design, PSC with fluorescent design shows a slightly lower J_{SC} and a reduced predicted temperature from the simulation (i.e., from 51.8 to 47.8 $^{\circ}\text{C}$). Benefiting from the lower working temperature, a higher V_{OC} for PSC with fluorescent design can be achieved, i.e., from 842 to 850 mV for PSCs without and with fluorescent design, respectively. To fully reveal the potential of down-conversion materials on this type of devices, an ideal case (QY = 100%) is also considered, which demonstrates a higher device efficiency of 21.61% and a lower working temperature of 48.4 $^{\circ}\text{C}$. Here, we need to point out that for case with Fluor, the quantum yield (QY) of the down-conversion material was non-ideal as shown in Figure S2 (Supporting Information); while for case with an ideal Fluor, a QY = 100% at the considered wavelengths was assumed. Therefore, devices with an ideal Fluor, as can be seen from Figure S4 (Supporting Information), could excite more photons and thus higher thermalization losses at 500–700 nm compared with the counterparts with a non-ideal Fluor. However, devices with an ideal Fluor show higher J_{SC} and PCE as compensation for a slightly higher operating temperature as shown in Figure 5d. This means that the down-conversion strategy has the potential to simultaneously reduce thermal loss, lower operating temperature, and promote device performance. In addition, it is worth noting that the down-conversion is proposed to simply serve as a proof-of-concept thermal management strategy, and whether it can be industrialized needs further confirmation in the future.

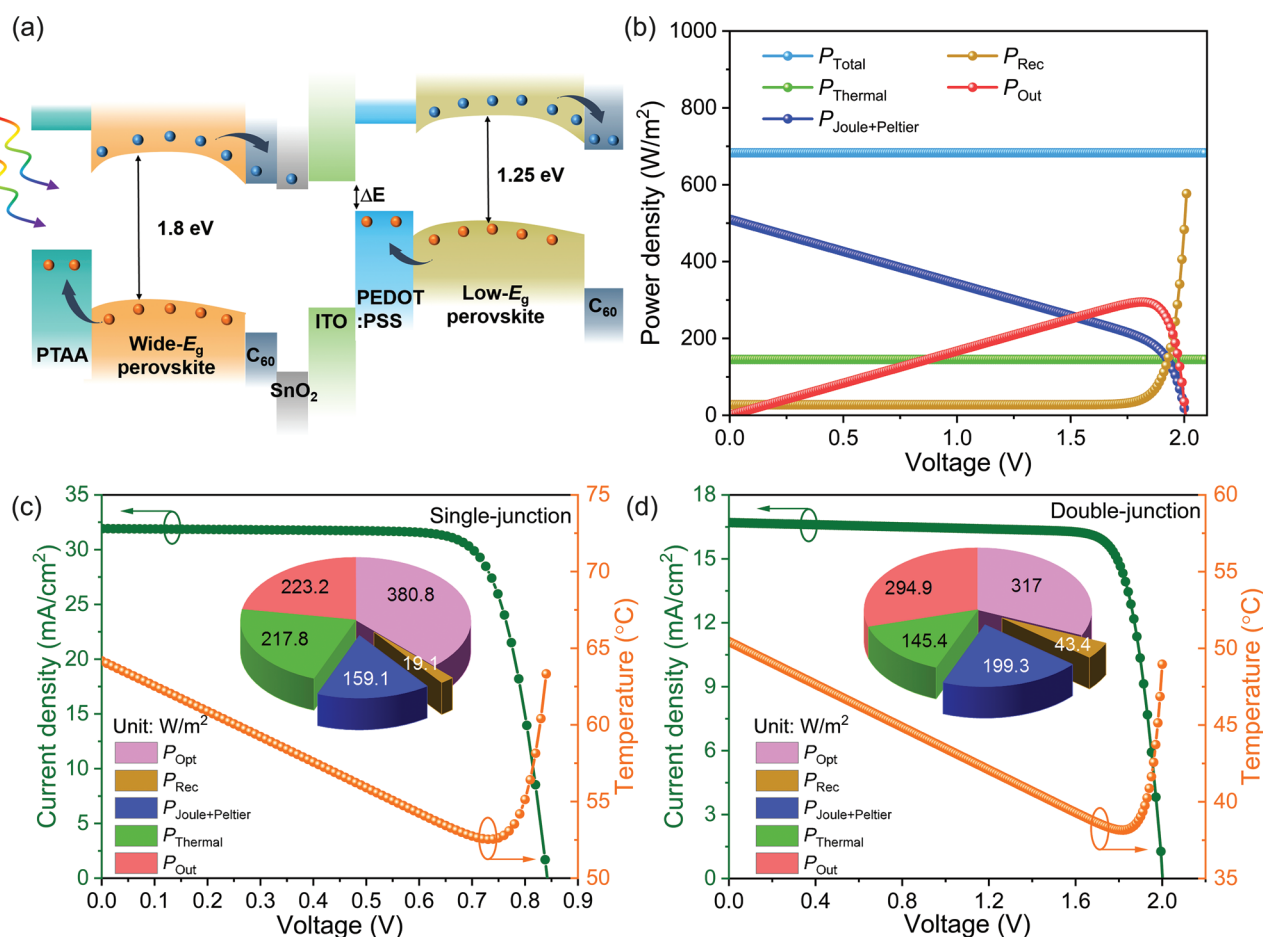


Figure 6. Microscopic quantitative analysis of double-junction tandem PSC. a) Schematic diagram of a tandem PSC consisted of two perovskite sub-cells. b) Power density curves of the different heat conversion contributions. c, d) J - V curves and temperature plots under the various biases of the single- and double-junction tandem PSCs, respectively, where the microscopic energy conversion components at MPP are inserted in the figure. Here, P_{Opt} , P_{Rec} , $P_{\text{Joule+Peltier}}$, P_{Thermal} , and P_{Out} denote the power densities for optical loss, recombination, intrinsic loss (including Joule and Peltier losses), thermalization, and electrical output processes, respectively.

2.4. Energy Analysis and Manipulation of Tandem PSCs

As a promising alternative scheme, multi-junction configuration is also one of the most effective means to suppress thermodynamic losses for achieving high efficiency PV devices.^[44,45] Taking an example of a perovskite/perovskite tandem SC as shown in **Figure 6a**, we perform a microscopic quantitative analysis to reveal the inherent thermodynamic behavior of double-junction tandem SCs. The energy distributions of this type of tandems under various forward biases are displayed in **Figure 6b**, which are consistent with that of single-junction PSC in addition to the differences in specific values. Moreover, the corresponding J - V and temperature curves as well as energy distributions of single- and double-junction tandem PSCs at MPP conditions are illustrated **Figure 6c,d**, respectively. We can conclude from these results that: 1) due to the more reasonable use of absorbed light, the thermalization loss is significantly reduced from 217.8 W m^{-2} (single-junction) to 145.4 W m^{-2} (tandem), confirming the feasibility of tandem design to reduce the thermalization loss;^[16] 2) the tandem PSC produces a high energy output of 294.9 W m^{-2} , which is much higher than

223.2 W m^{-2} inherent to the single-junction system; 3) the contributions of Joule, Peltier and recombination heats of the tandem devices are slightly increased compared with the single-junction devices, which can be attributed to the fact that the tandem devices produce higher optical absorption than that of the single-junction devices; 4) thanks to the lower heat generation and higher energy utilization, the double-junction tandem devices receive a lower predicted temperature of $37.9 \text{ }^{\circ}\text{C}$ at MPP, much lower than that of the single-junction devices ($51.8 \text{ }^{\circ}\text{C}$).

2.5. Optimal Schemes of Single-Junction and Tandem PSCs

In this section, we summarize the energy loss types and provide the corresponding optimization strategies for a PV device as shown in **Figure 7a** with the purposes of minimizing thermodynamic loss and promoting device efficiency by accelerating heat dissipation and lowering device operating temperature. From the optical perspective, the effective light absorption of a PV cell can be further promoted via optical management strategies such as advanced light-trapping design and material

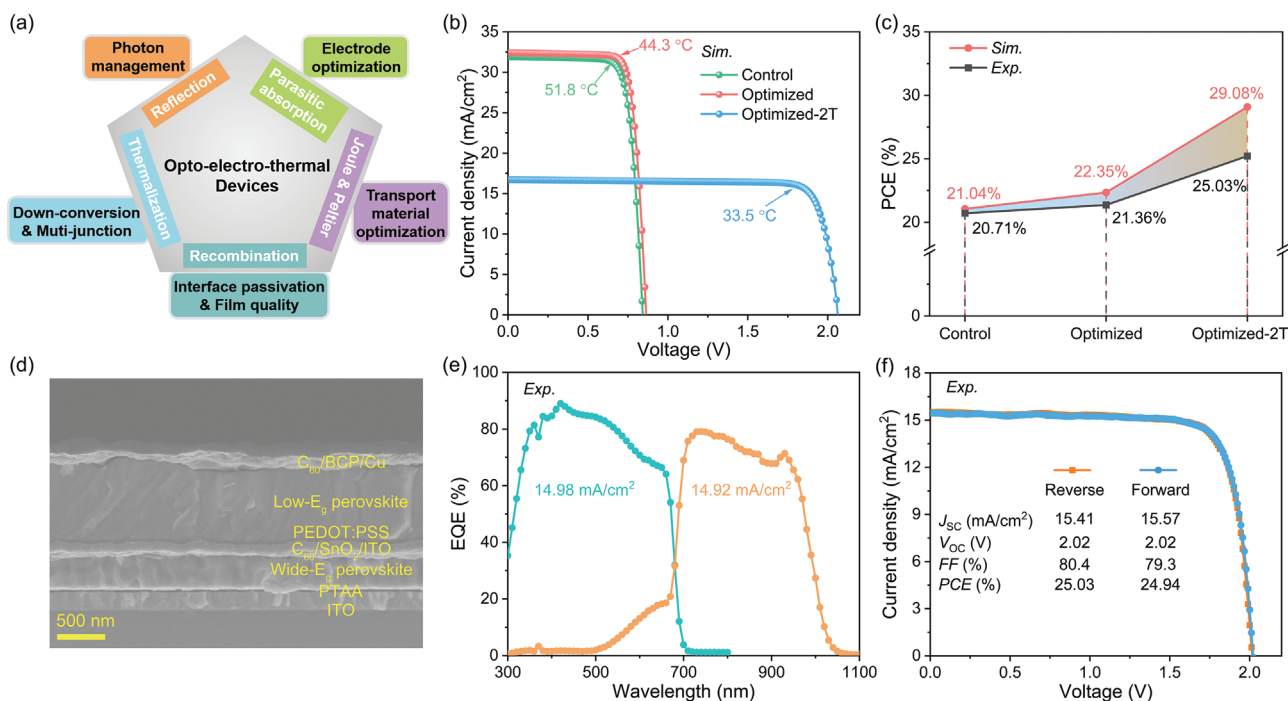


Figure 7. Heat management of a PV device and PCE improvement roadmap. a) Energy loss types and the corresponding optimization strategies of a PV device. b) Simulated $J-V$ characteristic curves for the control and optimized single-junction PSCs together with the tandem PSCs. c) Simulated and experimental PCE distributions of the related devices. d) Cross-sectional SEM image of the 2-T tandem PSC. e) Experimental EQE spectra, and f) $J-V$ curves of the 2-T tandem PSC.

screening to minimize parasitic absorption and reflection loss.^[19] From the electric viewpoint, high-efficiency PV device requires maximal power output and minimal carrier recombination, which can be realized by means of energy band alignment, film quality improvement, and interface passivation engineering,^[46–48] etc. In this case, recombination, Peltier and Joule heats can be thus well controlled. As for the thermodynamic scope, the effective strategies including multi-junction structure and down-conversion design should be employed to accelerate the heat dissipation and reduce the operating temperature of devices. Understandably, the thermal effect can be directly related to the initial efficiency of PSCs, however, the long-term stability of the device relies mostly on the material properties; nevertheless, the favorable thermal management strategies are beneficial for long-term stability of the device because they are beneficial for suppressing the thermal-induced stability degeneration.

Based on the above analyses, the single-junction PV devices can be further optimized. As displayed in Figure 7b,c, by tailoring the energy band levels of ETLs and HTLs and increasing the convective coefficient from 12 to 18 W m⁻² K⁻¹, the simulated PCE of the single-junction PSC can be improved from 21.04% to 22.35%, and the predicted temperature can be reduced from 51.8 to 44.3 °C. Moreover, the tandem PSCs are also evaluated, theoretically predicting a higher PCE of 29.08% and a lower operating temperature of 33.5 °C. To further confirm the simulation conclusions, we implement the corresponding experiments, where the fabrication method is presented in the Supporting Information. Here, to accelerate heat dissipation, we introduced a physical cooling method by

using an air fan during the test to improve the thermal convection coefficient (h). In addition, PEDOT:PSS was modified by PH buffer (*tris*-(hydroxymethyl)-aminomethane) to adjust its energy level. The corresponding $J-V$ characteristic curves, electrical parameters distributions and scanning electron microscopy (SEM) images are shown in Figures S5–S7 (Supporting Information), respectively. As well, the photovoltaic performance statistical results that are based on 25 independent devices fabricated in different batches verify a very good fabrication reproducibility in our experiment. Furthermore, the monolithic 2-T all-perovskite tandem PSCs are also fabricated as demonstrated in Figure 7d–f. The detailed device structure is consisted of glass/ITO/PTAA/1.8 eV wide- E_g perovskite/ C_{60} /SnO₂/ITO/PEDOT:PSS/1.25 eV low- E_g perovskite/ C_{60} /BCP/Cu, which can be verified by the cross-sectional SEM image as shown in Figure 7d. The EQE-integrated J_{SC} s of the top and bottom sub-cells in Figure 7e are determined to be 14.98 and 14.92 mA cm⁻², respectively, which are consistent with the $J-V$ results in Figure 7f. As a result, this type of tandem device delivers a PCE of 25.03% (24.94%) under a reverse (forward) voltage scanning. In addition, the time-dependent power output measurement using the maximum power point tracking (MPPT) protocol was provided, where the stable PCE of ≈24% is realized for 2-T all perovskite tandem device. It indicated that the device did not show any performance drop during the test >4000 s (Figure S8, Supporting Information). Moreover, we provide the real working temperatures measured from experiments for both single-junction and tandem PSCs as shown in Figures S9 and S10 (Supporting Information). Taking MPP condition as an example, the single-junction low- E_g and 2-T

tandem PSCs showed the measured temperatures of 42.79 and 34.02 °C, respectively, which are consistent with the simulation results (i.e., 44.3 and 33.5 °C).

Here, we need to emphasize that the experimental PCEs that we presented still lag far behind the simulation, which is particularly relevant for the tandem devices. The large gap between experimental and simulated PCEs is mainly due to the imperfect preparation process and device integration, which thus relies on the ongoing progresses such as optical design/matching, film quality improvement, functional layer screening/modification, and interface passivation, etc., to further promote the device performance. However, for the purpose of concept verification, this still supports the conclusions that we presented in this study.

3. Conclusion

In conclusion, we conducted a rigorous OET model for a PV cell and tandem to clarify the heat generation, dissipation, and manipulation mechanisms behind the devices. Taking a low- E_g PSC as an example, we addressed the microscopic energy conversion processes by considering the contributions from thermalization, Joule, Peltier, bulk/interface recombination heats, and proposed two feasible strategies, i.e., convective and radiative cooling, to accelerate heat dissipation. The simulated results reveal that the Peltier and thermalization heat losses account for a large part of energy losses. By tailoring the energy band levels with the suitable HTLs and ETLs, the Peltier losses can be effectively regulated. With the introduction of a YAG:Ce down-conversion material, the thermalization heat loss was effectively reduced from the initial 217.8 to 194.8 W m⁻², and the corresponding device temperature was reduced from 51.8 to 47.8 °C. In addition, a microscopic quantitative analysis for 2-T tandem SCs was performed to reveal their inherent thermodynamic behavior, which suggests that apart from the high-efficiency potential, the presence of the tandem SCs could intrinsically reduce thermalization loss and thus lower the operating temperature (≈ 33.5 °C at MPP). Moreover, to support the simulation conclusions, the single-junction and tandem PSCs were experimentally prepared with the PCEs of 21.36% and 25.03%, respectively. In general, the simulation and experimental results demonstrated in this study concerning the heat generation, dissipation, and manipulation mechanisms for both single-junction PV cells and tandems, shed new light on the intrinsic physical behaviors of energy conversion/dissipation processes, providing powerful guidance for designing high-efficiency and low-temperature PV devices.

Supporting Information

Supporting Information is available from the Wiley Online Library or from the author.

Acknowledgements

This work was financially supported by the National Key Research and Development Program of China (2022YFB4200900), the National

Natural Science Foundation of China (nos. 61875143, 62005188, and 62120106001), Natural Science Foundation of Jiangsu Province (BK20190825), Postgraduate Research & Practice Innovation Program of Jiangsu Province (KYCX22_3188), and Priority Academic Program Development (PAPD) of Jiangsu Higher Education Institutions.

Conflict of Interest

The authors declare no conflict of interest.

Data Availability Statement

The data that support the findings of this study are available from the corresponding author upon reasonable request.

Keywords

opto–electro–thermal simulations, perovskite solar cells, tandems, temperature effect, thermal manipulations

Received: October 30, 2022

Revised: December 24, 2022

Published online:

- [1] Best Research-Cell Efficiency Chart <https://www.nrel.gov/pv/cell-efficiency.html> (accessed: August 2022).
- [2] Y. Zhan, X. Li, Y. Li, *IEEE J. Sel. Top. Quantum Electron.* **2013**, 19, 1.
- [3] A. S. M. Mohsin, M. Mobashera, A. Malik, M. Rubaiat, M. Islam, *J. Opt.* **2020**, 49, 523.
- [4] K. Deng, Z. Liu, M. Wang, L. Li, *Adv. Funct. Mater.* **2019**, 29, 1900830.
- [5] M. Kim, J. Jeong, H. Lu, T. K. Lee, F. T. Eickemeyer, Y. Liu, I. W. Choi, S. J. Choi, Y. Jo, H.-B. Kim, S.-I. Mo, Y.-K. Kim, H. Lee, N. G. An, S. Cho, W. R. Tress, S. M. Zakeeruddin, A. Hagfeldt, J. Y. Kim, M. Grätzel, D. S. Kim, *Science* **2022**, 375, 302.
- [6] A. Al-Ashouri, E. Köhnen, B. Li, A. Magomedov, H. Hempel, P. Caprioglio, J. A. Márquez, A. B. Morales Vilches, E. Kasparavicius, J. A. Smith, N. Phung, D. Menzel, M. Grischek, L. Kegelmann, D. Skroblin, C. Gollwitzer, T. Malinauskas, M. Jošt, G. Matič, B. Rech, R. Schlatmann, M. Topič, L. Korte, A. Abate, B. Stannowski, D. Neher, M. Stollerfoht, T. Unold, V. Getautis, S. Albrecht, *Science* **2020**, 370, 1300.
- [7] M. A. Mahmud, J. Zheng, S. Tang, G. Wang, J. Bing, A. D. Bui, J. Qu, L. Yang, C. Liao, H. Chen, S. P. Bremner, H. T. Nguyen, J. Cairney, A. W. Y. Ho-Baillie, *Adv. Energy Mater.* **2022**, 12, 2201672.
- [8] Q. Jiang, Y. Zhao, X. Zhang, X. Yang, Y. Chen, Z. Chu, Q. Ye, X. Li, Z. Yin, J. You, *Nat. Photonics* **2019**, 13, 460.
- [9] Y. Lin, Y. Bai, Y. Fang, Z. Chen, S. Yang, X. Zheng, S. Tang, Y. Liu, J. Zhao, J. Huang, *J. Phys. Chem. Lett.* **2018**, 9, 654.
- [10] C. C. Boyd, R. Cheacharoen, K. A. Bush, R. Prasanna, T. Leijtens, M. D. McGehee, *ACS Energy Lett.* **2018**, 3, 1772.
- [11] K. Choi, J. Lee, H. Choi, G.-W. Kim, H. I. Kim, T. Park, *Energy Environ. Sci.* **2020**, 13, 5059.
- [12] N. Yang, F. Pei, J. Dou, Y. Zhao, Z. Huang, Y. Ma, S. Ma, C. Wang, X. Zhang, H. Wang, C. Zhu, Y. Bai, H. Zhou, T. Song, Y. Chen, Q. Chen, *Adv. Energy Mater.* **2022**, 12, 2200869.
- [13] F. Pei, N. Li, Y. Chen, X. Niu, Y. Zhang, Z. Guo, Z. Huang, H. Zai, G. Liu, Y. Zhang, Y. Bai, X. Zhang, C. Zhu, Q. Chen, Y. Li, H. Zhou, *ACS Energy Lett.* **2021**, 6, 3029.
- [14] T. Moot, J. B. Patel, G. McAndrews, E. J. Wolf, D. Morales, I. E. Gould, B. A. Rosales, C. C. Boyd, L. M. Wheeler, P. A. Parilla,

- S. W. Johnston, L. T. Schelhas, M. D. McGehee, J. M. Luther, *ACS Energy Lett.* **2021**, *6*, 2038.
- [15] E. Aydin, T. G. Allen, M. De Bastiani, L. Xu, J. Ávila, M. Salvador, E. Van Kerschaver, S. De Wolf, *Nat. Energy* **2020**, *5*, 851.
- [16] Y. An, T. Ma, X. Li, *Sol. RRL* **2021**, *5*, 2100199.
- [17] L. C. Hirst, N. J. Ekins-Daukes, *Prog. Photovoltaics* **2011**, *19*, 286.
- [18] A. Shang, X. Li, *Adv. Mater.* **2017**, *29*, 1603492.
- [19] Y. An, C. Wang, G. Cao, X. Li, *ACS Nano* **2020**, *14*, 5017.
- [20] Y. An, C. Sheng, X. Li, *Nanoscale* **2019**, *11*, 17073.
- [21] X. Li, N. P. Hylton, V. Giannini, K.-H. Lee, N. J. Ekins-Daukes, S. A. Maier, *Prog. Photovoltaics* **2013**, *21*, 109.
- [22] X. Li, N. P. Hylton, V. Giannini, K.-H. Lee, N. J. Ekins-Daukes, S. A. Maier, *Opt. Express* **2011**, *19*, A888.
- [23] G. K. Wachutka, *IEEE Trans. Comput.* **1990**, *9*, 1141.
- [24] P. B. M. Wolbert, G. K. M. Wachutka, B. H. Krabbenborg, T. J. Mouthaan, *IEEE Trans. Comput.* **1994**, *13*, 293.
- [25] N. Brinkmann, G. Micard, Y. Schiele, G. Hahn, B. Terheiden, *Phys. Status Solidi RRL* **2013**, *7*, 322.
- [26] Z. Yu, X. Chen, S. P. Harvey, Z. Ni, B. Chen, S. Chen, C. Yao, X. Xiao, S. Xu, G. Yang, Y. Yan, J. J. Berry, M. C. Beard, J. Huang, *Adv. Mater.* **2022**, *34*, 2110351.
- [27] J. Tong, Q. Jiang, A. J. Ferguson, A. F. Palmstrom, X. Wang, J. Hao, S. P. Dunfield, A. E. Louks, S. P. Harvey, C. Li, H. Lu, R. M. France, S. A. Johnson, F. Zhang, M. Yang, J. F. Geisz, M. D. McGehee, M. C. Beard, Y. Yan, D. Kuciauskas, J. J. Berry, K. Zhu, *Nat. Energy* **2022**, *7*, 642.
- [28] R. Lin, J. Xu, M. Wei, Y. Wang, Z. Qin, Z. Liu, J. Wu, K. Xiao, B. Chen, S. M. Park, G. Chen, H. R. Atapattu, K. R. Graham, J. Xu, J. Zhu, L. Li, C. Zhang, E. H. Sargent, H. Tan, *Nature* **2022**, *603*, 73.
- [29] C. Li, Z. Song, D. Zhao, C. Xiao, B. Subedi, N. Shrestha, M. M. Junda, C. Wang, C.-S. Jiang, M. Al-Jassim, R. J. Ellingson, N. J. Podraza, K. Zhu, Y. Yan, *Adv. Energy Mater.* **2019**, *9*, 1803135.
- [30] P. Singh, N. M. Ravindra, *Sol. Energy Mater. Sol. Cells* **2012**, *101*, 36.
- [31] W. Tress, K. Domanski, B. Carlsen, A. Agarwalla, E. A. Alharbi, M. Graetzel, A. Hagfeldt, *Nat. Energy* **2019**, *4*, 568.
- [32] L. Zhu, A. Raman, K. X. Wang, M. A. Anoma, S. Fan, *Optica* **2014**, *1*, 32.
- [33] K. Wang, G. Luo, X. Guo, S. Li, Z. Liu, C. Yang, *Sol. Energy* **2021**, *225*, 245.
- [34] M. Koehl, S. Hamperl, M. Heck, *Prog. Photovoltaics* **2016**, *24*, 1194.
- [35] W. Zhang, L. Huang, W. Zheng, S. Zhou, X. Hu, J. Zhou, J. Li, J. Liang, W. Ke, G. Fang, *Nano Energy* **2022**, *96*, 107078.
- [36] K. Deepthi Jayan, V. Sebastian, *Sol. Energy* **2021**, *217*, 40.
- [37] Z. Yang, W. Yang, X. Yang, J. C. Greer, J. Sheng, B. Yan, J. Ye, *Energy Environ. Sci.* **2020**, *13*, 1753.
- [38] S. Min, S. Jeon, K. Yun, J. Shin, *ACS Photonics* **2022**, *9*, 1196.
- [39] R. A. Yalçın, E. Blandre, K. Joulain, J. Drévilion, *ACS Photonics* **2020**, *7*, 1312.
- [40] T. Trupke, M. A. Green, P. Würfel, *J. Appl. Phys.* **2002**, *92*, 1668.
- [41] Z. Liu, S. Liu, K. Wang, X. Luo, *Appl. Opt.* **2010**, *49*, 247.
- [42] X. Zhang, J. Qiu, X. Li, J. Zhao, L. Liu, *Appl. Opt.* **2020**, *59*, 2337.
- [43] X. Zhang, J. Qiu, J. Zhao, X. Li, L. Liu, *J. Quant. Spectrosc. Radiat. Transfer* **2020**, *252*, 107063.
- [44] C. Wang, Y. Zhao, T. Ma, Y. An, R. He, J. Zhu, C. Chen, S. Ren, F. Fu, D. Zhao, X. Li, *Nat. Energy* **2022**, *7*, 744.
- [45] L. Li, Y. Wang, X. Wang, R. Lin, X. Luo, Z. Liu, K. Zhou, S. Xiong, Q. Bao, G. Chen, Y. Tian, Y. Deng, K. Xiao, J. Wu, M. I. Saidaminov, H. Lin, C.-Q. Ma, Z. Zhao, Y. Wu, L. Zhang, H. Tan, *Nat. Energy* **2022**, *7*, 708.
- [46] S. Hu, M. A. Truong, K. Otsuka, T. Handa, T. Yamada, R. Nishikubo, Y. Iwasaki, A. Saeki, R. Murdey, Y. Kanemitsu, A. Wakamiya, *Chem. Sci.* **2021**, *12*, 13513.
- [47] S. Hu, K. Otsuka, R. Murdey, T. Nakamura, M. A. Truong, T. Yamada, T. Handa, K. Matsuda, K. Nakano, A. Sato, K. Marumoto, K. Tajima, Y. Kanemitsu, A. Wakamiya, *Energy Environ. Sci.* **2022**, *15*, 2096.
- [48] G. Kapil, T. Bessho, Y. Sanehira, S. R. Sahamir, M. Chen, A. K. Baranwal, D. Liu, Y. Sono, D. Hirotani, D. Nomura, K. Nishimura, M. A. Kamarudin, Q. Shen, H. Segawa, S. Hayase, *ACS Energy Lett.* **2022**, *7*, 966.